Photofragmentation dynamics of N,N-dimethylformamide following excitation at 193 nm

M. Laura Lipciuc, Sara H. Gardiner, Tolga N. V. Karsili, Jason W. L. Lee, David Heathcote, Michael N. R. Ashfold, and Claire Vallance

Citation: The Journal of Chemical Physics **147**, 013941 (2017); doi: 10.1063/1.4983704
View online: https://doi.org/10.1063/1.4983704
View Table of Contents: http://aip.scitation.org/toc/jcp/147/1
Published by the American Institute of Physics

Photofragmentation dynamics of *N*,*N*-dimethylformamide following excitation at 193 nm

M. Laura Lipciuc,[1] Sara H. Gardiner,[1] Tolga N. V. Karsili,[2] Jason W. L. Lee,[1] David Heathcote,[1] Michael N. R. Ashfold,[2] and Claire Vallance[1,a)]
[1]*Department of Chemistry, Chemistry Research Laboratory, University of Oxford, 12 Mansfield Road, Oxford OX1 3TA, United Kingdom*
[2]*School of Chemistry, University of Bristol, Cantocks Close, Bristol BS8 1TS, United Kingdom*

(Received 25 February 2017; accepted 6 May 2017; published online 26 May 2017)

N,*N*-dimethylformamide, $HCON(CH_3)_2$, is a useful model compound for investigating the peptide bond photofragmentation dynamics. We report data from a comprehensive experimental and theoretical study into the photofragmentation dynamics of *N*,*N*-dimethylformamide in the gas phase at 193 nm. Through a combination of velocity-map imaging and hydrogen atom Rydberg tagging photofragment translational spectroscopy we have identified two primary fragmentation channels, namely, fission of the N—CO "peptide" bond and $N—CH_3$ bond fission leading to the loss of CH_3. The possible fragmentation channels leading to the observed products are rationalised with recourse to CASPT2 calculations of the ground and first few excited-state potential energy curves along the relevant dissociation coordinates, and the results are compared with the data from previous experimental and theoretical studies on the same system. *Published by AIP Publishing.* [http://dx.doi.org/10.1063/1.4983704]

I. INTRODUCTION

Photofragmentation studies on amide systems are of key interest as a stepping stone to understanding the behaviour of energised peptide bonds within proteins. In addition to providing insight into photostability and photodamage mechanisms in biomolecules, such studies also have the potential to inform mass spectrometric studies of the molecular structure, in which UV photolysis is increasingly being used to induce fragmentation.[1] The present study focuses on the 193 nm photofragmentation of *N*,*N*-dimethylformamide (*N*,*N*-DMF), a molecule that has been considered previously in a number of experimental[2,3] and theoretical[4,5] studies as a useful model compound for investigating the peptide bond fragmentation dynamics. In common with peptide bonds in proteins, *N*,*N*-DMF has a planar structure (see Fig. 1), as a consequence of the partial double bond character of the N—CO "peptide" bond that results from partial conjugation of the lone pair on the nitrogen atom into the C=O π^* system.

The long wavelength part of the UV absorption spectrum of *N*,*N*-DMF shows two overlapping bands peaking at 197.4 nm and 162.1 nm, respectively. Previous theoretical studies have identified singlet states attributable to $\pi^* \leftarrow n$ transitions in which an oxygen $2p_y$ lone-pair electron and a nitrogen $2p\pi$ lone-pair electron, respectively, are promoted to the C=O π^* antibonding orbital.[6–9] The photolysis wavelength of 193 nm employed in the present study is close to the peak of the first of the two absorption bands. However, previous experimental studies[3,10] have indicated that both transitions can be excited at this wavelength and result in the fragmentation of the parent molecule via cleavage of the N—CO "peptide" bond, one of the $N—CH_3$ bonds, or possibly the aldehydic C—H bond.

Focusing first on the "peptide" bond fragmentation channels accessible at 193 nm, three different pairs of electronic states are accessible on energetic grounds for the $HCO + N(CH_3)_2$ products. Both products can be formed in their ground states (i.e., HCO $[\tilde{X}] + N(CH_3)_2$ $[\tilde{X}]$), or either the HCO or $N(CH_3)_2$ product can be formed in its first excited state (i.e., HCO $[\tilde{A}]$ or $N(CH_3)_2$ $[\tilde{A}]$). The amount of energy available to be released into product translation is different in each case, and therefore experimental measurements of the photofragment velocity distributions offer a potential route to establishing the branching ratios for the formation of each of the three possible product pairs. These in turn provide insight into the details and topographies of the potential energy surfaces that control the fragmentation dynamics.

Forde *et al.*[2,3] performed such a study in the late 1990s. A traditional photofragment translational spectroscopy method was employed, in which the time-of-flight profiles for the selected photofragments were recorded by electron ionization and quadrupole mass spectrometric detection. The authors identified contributions from three dissociation pathways following excitation at 193 nm. Two involved N—CO "peptide" bond cleavage, leading to the formation of ground-state HCO[$\tilde{X}$] radicals partnered by $N(CH_3)_2$ radicals in both their $\tilde{X}$ and $\tilde{A}$ states. These products showed an anisotropic recoil velocity distribution, characterised by a recoil anisotropy parameter $\beta = 1.2 \pm 0.2$. This was thought to indicate prompt bond rupture relative to the parent rotational period, following excitation via a transition with an associated dipole moment aligned preferentially parallel to the breaking bond. The limited available translational energy resolution precluded the determination of separate β parameters for each of the

a)Author to whom correspondence should be addressed: claire.vallance@chem.ox.ac.uk

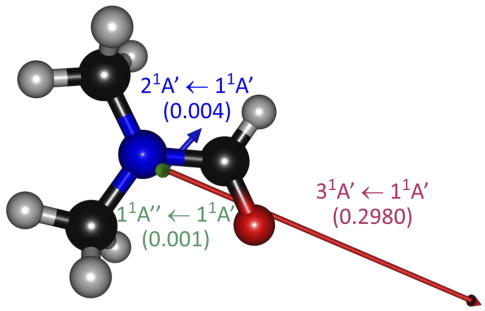

FIG. 1. The molecular structure of *N*,*N*-dimethylformamide. The calculated transition dipole moments for excitation from the $1^1A'$ ground state to the $1^1A''$ (S_1), $2^1A'$ (S_2), and $3^1A'$ (S_3) states are shown as green, blue, and red arrows, respectively (see Sec. II B for a description of these calculations).

two product channels. The third dissociation pathway identified was N—CH_3 bond fission, which was estimated to account for around one-third of the measured fragmentation yield. Unfortunately, problems with overlapping time-of-flight signals and interfering signals from CH_3^+ ions formed by the cracking of larger fragments within the ionization region of the detector prevented determination of the associated β parameter. The possible participation of fragmentation channels involving the loss of an H atom could not be assessed on account of the high background signals at this mass.

Forde *et al.*[2,3] also reported preliminary results from *ab initio* electronic structure calculations that were performed in order to aid interpretation of their experimental data. These were followed by two further theoretical studies by Liu *et al.*[4] and Eckert-Maksić and Antol.[5] Liu *et al.* employed state-averaged complete active space self-consistent field (SA-CASSCF) methods to compute the ground (S_0) and first excited singlet (S_1) and triplet (T_1) adiabatic potential energy surfaces of *N*,*N*-DMF and the regions of the configuration space in which these surfaces intersect. They concluded that most of the N—CO "peptide" bond cleavage following excitation at 193 nm occurs on the S_1 surface, with some contribution from the T_1 surface following intersystem crossing (ISC) from S_1, both leading to the formation of HCO and $N(CH_3)_2$ products in their electronic ground states. The triplet state was also thought to dissociate along a CH_3-loss coordinate to give $HCONCH_3 + CH_3$ products. The later study by Eckert-Maksić and Antol[5] employed similar SA-CASSCF calculations to locate stationary points (energy minima and saddle points) and minima on the crossing seams linking the S_0, S_1, and S_2 surfaces. These were then used in the direct trajectory surface hopping calculations to explore possible routes to "peptide" bond fission following the 193 nm photoexcitation of *N*,*N*-DMF. We will explore the conclusions reached in these various theoretical treatments in Sec. III.

In the present work, we report a new experimental study of the 193 nm photofragmentation dynamics of *N*,*N*-dimethylformamide employing "universal" vacuum ultraviolet (VUV) photoionization and velocity-map imaging of the resulting photofragments. The velocity-map images provide much higher angular resolution than the earlier photofragment translational spectroscopy measurements of Forde *et al.*,[2,3] though these measurements were state-of-the-art for their time. The present imaging studies are also less prone to complications associated with the overlap of time-of-flight signals from different ion masses. The much lower ionization energy employed in our experiments (a 10.48 eV laser photon rather than a 200 eV electron) also circumvents many of the challenges associated with cracking of photofragments into smaller species at the detector, allowing better reconstruction of the signals for intact photofragments. Possible hydrogen atom elimination channels have also been investigated via separate hydrogen Rydberg atom photofragment translational spectroscopy measurements. The analysis of the time-of-flight spectra and the photofragment translational energy and angular distributions extracted from the data, supported by new *ab initio* calculations of the energetic pathways for the energetically accessible fragmentation processes, allows us to revisit the earlier conclusions drawn by Forde *et al.*,[2,3] to confirm many of their findings, and to address some of the open questions posed by their work and the theoretical studies that followed.

II. METHODS

A. Experiment

The velocity-map imaging experimental setup has been described in detail elsewhere.[11,12] The following is a brief description of the experimental conditions. A seeded beam (seeding ratio ~0.2%) of ~4 mbar *N*,*N*-dimethylformamide (Sigma-Aldrich, >99.8%) in 2 bars of He (BOC, >99.9%) undergoes a supersonic expansion through a pulsed solenoid valve (Parker Hannifin, Series 9) into vacuum to generate the molecular beam. Within the interaction region, the molecular beam is intersected at right angles by two counter-propagating linearly polarized laser beams of wavelengths 193 nm (from a Neweks PSX-100 ArF excimer laser) and 118.2 nm (generated by tripling the 355 nm output of a Continuum Surelite I Nd:YAG laser in a phase-matched mixture of Xe and Ar[13–15]), separated in time by about 20 ns. The *N*,*N*-DMF molecules are photolysed by a 193 nm photon, and the resulting neutral dissociation products are ionized by a VUV photon. The nascent ions are velocity-mapped along a 48.2 cm flight tube onto a position sensitive detector (Photonis) consisting of a pair of microchannel plates coupled to a P47 phosphor screen. The microchannel plates are time-gated to the arrival time of the ion of interest using a high-voltage pulse generator (Photek GM-MCP-2), and images from the phosphor are acquired with an intensified CCD camera (Photonic Science MiniIDI) via a LabVIEW interface. Images are accumulated over several tens of thousands of laser pump-probe cycles in order to achieve an acceptable signal-to-noise ratio. Time-of-flight mass spectra are recorded by counting the number of ions detected as a 20 ns time-gate applied to the microchannel plates is swept across the ion arrival time range of interest. Time-of-flight spectra and velocity-map images are recorded for pump-only, probe-only, and pump-probe laser combinations, and the single-laser signals are subtracted from the two-laser signals to give the true pump-probe signals, corresponding to the photofragments generated by the 193 nm photolysis that

are then ionized by the 118 nm probe laser. The assignment of the various peaks in the time-of-flight spectra was confirmed by recording similar spectra for *N*,*N*-DMF-d_7 and observing the expected changes in the mass-to-charge ratio for each fragment.

The images were processed using the BASEX software package[16] in order to obtain the speed and angular distributions of the various photofragments. The measured product velocities were calibrated using images of the atomic oxygen atoms of known velocity produced in the multiphoton dissociation and ionization of molecular oxygen at 225 nm.[17]

In order to investigate the hydrogen loss channels from *N*,*N*-DMF, H-atom Rydberg tagging measurements have been performed. The instrument has been described in detail previously.[18] In brief, a pulsed molecular beam comprising *N*,*N*-DMF (Sigma Aldrich, >99%, room temperature vapor pressure) in ~1 bar of Ar was expanded through a pulsed valve and skimmed prior to photolysis at 193 nm. H atoms formed in this interaction region were probed by the two-photon (121.6 nm + 366 nm) double resonant excitation via the 2*p* state to a high *n* Rydberg state. Rydberg atoms that recoil along the axis orthogonal to the plane containing the molecular beam and the photolysis/probe laser beams traverse a flight tube to a detector, where their times-of-flight are recorded. An extraction field of 50 V cm^{-1} applied across the interaction region ensures prompt removal of any H^+ ions created in the interaction region.

We note that in both sets of experiments we were able to obtain sufficiently high signal levels with a relatively low concentration of *N*,*N*-DMF within the molecular beam, in contrast to the much higher concentrations of around 8% employed by Forde *et al.*[3] We saw no significant evidence of clustering within the beam and did not need to heat the pulsed valve to prevent clusters from interfering with the signal from monomer fragmentation. The molecules undergoing photofragmentation in the present study are therefore likely to be significantly colder than in the previous experimental study of Forde *et al.*

B. Computational methodology

The ground-state optimized geometries and energies of neutral *N*,*N*-DMF and the various fragmentation products were obtained at the MP2/aug-cc-pVTZ level using the Gaussian09 software package.[19] In accord with the earlier studies discussed in Sec. I, products corresponding to the N—CO "peptide" bond fragmentation, CH_3 loss, and H-loss are all deduced to be energetically accessible at this wavelength.

Further calculations were performed using the MOLPRO Version 2010.1 computational package.[20] Using the MP2 optimised parent molecule geometry, vertical excitation energies and transition dipole moments for various neutral states of *N*,*N*-DMF were calculated using a state-averaged CASSCF method, employing the same aug-cc-pVTZ basis set as the initial geometry optimisation. The calculated transition dipole moments for vertical excitation to the $1^1A''$, $2^1A'$, and $3^1A'$ states are superimposed on the molecular structure of *N*,*N*-DMF shown in Fig. 1.

TABLE I. Vertical ionization energies for the photolysis products of *N*,*N*-dimethylformamide, calculated at the HF/aug-cc-pVTZ level with the P3 electron propagator theory correlation correction.

Species	Vertical ionization energy (eV)	Ionizable at 193 nm?	Ionizable at 118 nm?
$HCON(CH_3)_2$	9.59	No	Yes
$CON(CH_3)_2$	7.82	No	Yes
$HCONCH_3$	11.32	No	No
$N(CH_3)_2$	9.89	No	Yes
NC_2H_5	9.90	No	Yes
cis-$NCHCH_3$	7.93	No	Yes
trans-$NCHCH_3$	7.59	No	Yes
NH_4	4.44	Yes	Yes
CH_3	9.79	No	Yes
HCO	8.83	No	Yes
CO	13.79	No	No
H	13.60	No	No

The choice of the active space was a balance between attempting to describe all significant static correlation effects in the ground and excited electronic states in as even-handed a way as possible across the potential energy surface, and constraining the calculation to a manageable size. The active space comprises 12 electrons arranged in nine orbitals, namely, three σ and two σ^* orbitals, the in-plane oxygen p_y orbital, π and π^* orbitals centered around the C=O bond, and the nitrogen p_x orbital. Individual potential energy curves (PECs) along the N—CO "peptide," methylamino N—CH_3, and aldehydic C—H stretching coordinates were calculated at the CASPT2 level for the ground and various excited electronic states of the *N*,*N*-DMF neutral molecule. In each case, the remainder of the nuclear framework was frozen at the ground-state optimised geometry as the active coordinate was varied. A small imaginary level shift of 0.5 a.u. was applied to encourage convergence and to circumvent the presence of intruder states. Vertical excitation energies obtained from the CASPT2 calculations are in good agreement with the available experimental data.[6,7]

In addition to the potential energy surface calculations outlined above, vertical ionization energies for the various relevant molecular fragments were calculated at the HF/aug-cc-pVTZ level with the P3 electron propagator theory correlation correction. These are shown in Table I, and will be used to rationalise the presence or absence of signals from the various possible photolysis products following irradiation with the 193 nm pump and 118 nm (10.48 eV) probe radiation.

III. RESULTS AND DISCUSSION

A. Potential energy curves

Cuts through the CASPT2 potential energy surfaces calculated along (a) the N—CO bond, (b) a N—CH_3 bond, and (c) the aldehydic C—H stretch coordinate are shown in the three panels of Fig. 2. The vertical excitation energies to the first three singlet excited states, namely, the $1^1A''$, $2^1A'$, and $3^1A'$ states are ~5.0, ~6.0 and ~6.0 eV, respectively. All three states are therefore energetically accessible following

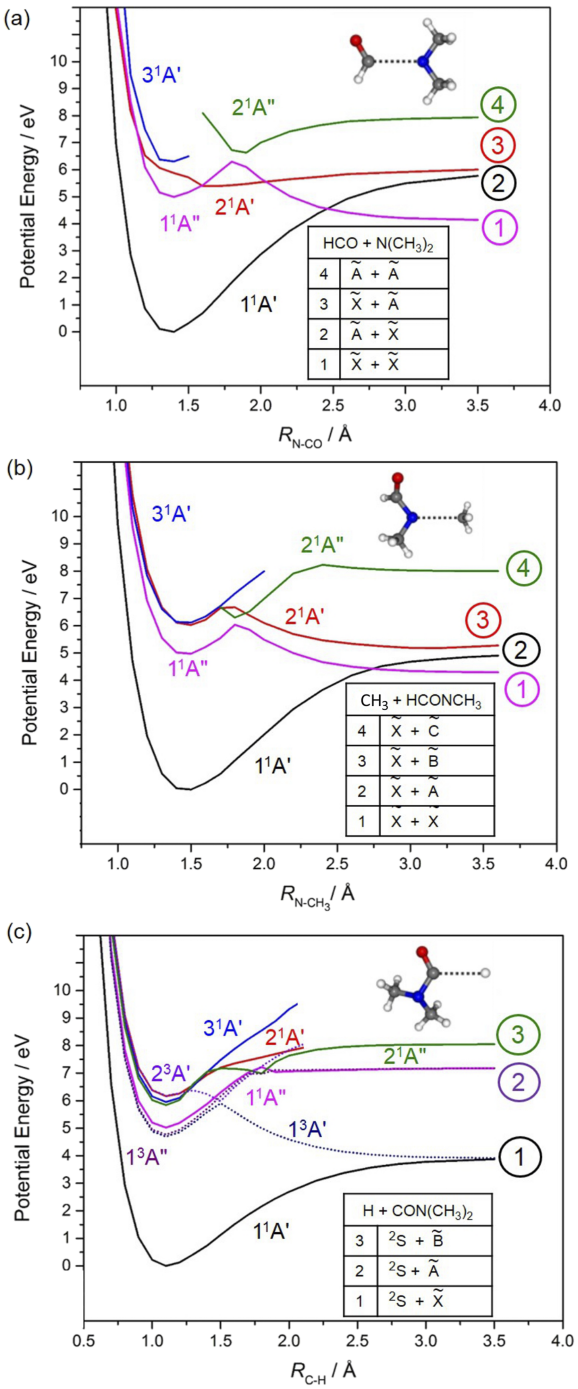

FIG. 2. Cuts through the adiabatic potential energy surfaces returned from CASPT2 calculations for dissociation of *N*,*N*-DMF along the (a) R_{N-CO}, (b) R_{N-CH_3}, and (c) aldehydic R_{C-H} bond extension coordinates. All other degrees of freedom were held fixed at their ground state equilibrium values during the calculations.

absorption of a 6.42 eV photon of 193 nm light. The calculated vertical excitation energy to the $1^1A''$ state is lower than that reported by Eckert-Maksić and Antol,[5] but still well above their reported value for the adiabatic transition to the (non-planar, *trans*-isomer) minimum energy geometry of the S_1 state. In accord with previous findings, the dominant orbital promotion associated with the $1^1A'' \leftarrow S_0$ transition in the Franck-Condon region is best described as $\pi^* \leftarrow n_O$. The $2^1A'$ and $3^1A'$ states returned by the present calculations are near degenerate; the former has a 3s Rydberg character, while the latter arises as a result of the $\pi^* \leftarrow \pi$ excitation. The very different spatial overlaps of the participating orbitals are reflected in the calculated oscillator strengths for the respective transitions from the S_0 state to the $1^1A''$, $2^1A'$, and $3^1A'$ states (0.001, 0.004, and 0.298, respectively). Thus, in contrast to the previous literature,[5] we identify the $3^1A'$ state as the "bright" $^1\pi\pi^*$ state. However, we recognise that this state is likely to be heavily mixed with, and predissociated by, the $2^1A'$ state and that nuclear motions on the latter potential energy surface will drive the fragmentations of current interest.

Focusing on the N—CO bond fission channel first, the potential energy curves in Fig. 2(a) show several curve crossings which develop into conical intersections once the planarity constraint is lifted. The calculated oscillator strengths imply predominant excitation to the $3^1A'$ state of *N*,*N*-DMF following excitation at 193 nm, but as noted above, we envisage rapid population transfer to the $2^1A'$ state. The $2^1A'$ state correlates with the first excited state of the $N(CH_3)_2$ radical upon N—CO bond extension. However, at extended N—CO bond lengths of around 2 Å, population on the $2^1A'$ surface can also couple to the repulsive $1^1A''$ potential, which correlates to ground-state products. The long-range part of this $1^1A''$ potential arises as a result of excitation from the delocalised π orbital spanning the nitrogen $2p_x$ orbital and C=O bond to a σ^* orbital localised along the N—CO bond. The potential energy curve for the resulting $^1\pi\sigma^*$ state shows a topography reminiscent of that of many other $(n/\pi)\sigma^*$ states,[21] even that for N—H bond fission in NH_3. In the planar limit, the state correlates asymptotically with ground-state products. However, a conical intersection with the $1^1A'$ (S_0) potential energy curve at $R_{N-CO} \sim 2.5$ Å has the result that any loss of planarity, for example, by pyramidalisation at the N atom, would favor dissociation to the electronically excited HCO products. Parent molecules initially excited to the $1^1A''$ state are likely to follow a similar sequence of radiationless transitions to those excited to the $2^1A'$ or $3^1A'$ state after initial coupling to the $2^1A'$ state via another conical intersection at shorter R_{N-CO} distances.

The calculated potential energy curves along the N—CH_3 stretch coordinate [Fig. 2(b)] show some similarities to those along the N—CO coordinate. Again, the curves for the $1^1A''$ and $2^1A'$ states correlate to the excited dissociation limits, in this case, associated with the formation of electronically excited $HCONCH_3$ radicals. The $2^1A'$ curve shows a barrier at $R_{N-CH_3} \sim 1.75$ Å, which we ascribe to the lower half of an avoided crossing with another state of $^1A'$ symmetry. The barrier height is almost certainly overestimated in the present (unrelaxed) calculations, so we can expect that the N—CH_3 bond fission is adiabatically allowed following excitation to the $3^1A'$ state at 193 nm and subsequent coupling to the $2^1A'$ potential. The $1^1A''$ and $2^1A'$ potential energy curves are both intersected at planar geometries by the repulsive part of the $1^1A''$ curve. The dominant orbital promotion associated with this dissociative region of the potential is from the same π orbital delocalised over the N—C=O spine as identified earlier to another σ^* orbital, this time localised along one N—CH_3 bond. The resulting state offers another possible

fragmentation pathway for population in the $2^1A'$ state, initiated by radiationless coupling (induced by an appropriate out-of-plane motion) at the conical intersection between the $2^1A'$ and $1^1A''$ states at $R_{N–CH_3} \sim 1.7$ Å. As was the case for dissociation along the N—CO coordinate, the $1^1A''$ potential energy curve forms a conical intersection with the S_0 curve at extended N—CH_3 bond lengths of ~2.75 Å. As noted earlier, this is reminiscent of the $(n/\pi)\sigma^*$-state-mediated dissociation[21] of NH_3 or CH_3NH_2. Dissociating *N*,*N*-DMF molecules following this pathway can either form ground-state radical products, if the last conical intersection is sampled at near planar geometries, or $CH_3 + HCONCH_3[\tilde{A}]$ products, if the adiabatic path (for non-planar geometries) is followed at the conical intersection.

Unlike the potential energy curves along the N—CO and N—CH_3 stretching coordinates, the singlet curves for the aldehydic C—H bond extension coordinate do not show a low-energy conical intersection at extended bond lengths and instead are more reminiscent of simpler systems such as H_2CO and HFCO.[22–25] The only dissociative potential energy curve along this coordinate is that of a $^3A'$ triplet state, formed by promoting an electron to a σ^* orbital localised on the breaking C—H bond. The importance of this channel will depend on the strength of the spin-orbit coupling from the photoexcited $1^1A''$, $2^1A'$, and/or $3^1A'$ states to the triplet manifold.

Continuing the analogy with H_2CO and HFCO suggests that we should also be cognisant of a possible molecular fragmentation channel yielding $(CH_3)_2NH + CO$ products. These are in fact the lowest energy dissociation products that could arise from photolysis of *N*,*N*-DMF,[2,3] but their formation would certainly involve passage over a substantial activation barrier. This pathway has not been investigated in the present computational work, but we note that the 8.24 eV ionization energy of the $(CH_3)_2NH$ product[26] is sufficiently low that any activity in this channel should be revealed by the present experiments.

B. Time-of-flight mass spectra and velocity-map images

Time-of-flight mass spectra were recorded for the photofragments generated following illumination of the sample by (a) only the 193 nm pump (UV) light, (b) only the 118 nm probe (VUV) light, and (c) both the 193 nm pump and 118 nm probe (UV/VUV) light. These spectra are shown in Fig. 3(a). The only signal generated by the pump laser alone is a small peak at $m/z = 44$, corresponding to the one-photon fragmentation of the peptide bond followed by the two-photon non-resonant ionization of the $N(CH_3)_2$ product within the same laser pulse. Single-photon ionization can be ruled out on the basis that with a calculated vertical ionization energy of 9.89 eV, the total energy available to the photolysis products is insufficient for even the most highly internally excited $N(CH_3)_2$ products to be ionized by a single photon at 193 nm. The probe laser alone generates a large peak at the parent ion mass, $m/z = 73$, together with peaks at $m/z = 30$, 42, 44, 58, 70, and 72 corresponding to the dissociative ionization products. These can be assigned as $C_2H_6^+$, $NC_2H_4^+$, $N(CH_3)_2^+$, $HCONCH_3^+$, and various H-atom-loss products, respectively.

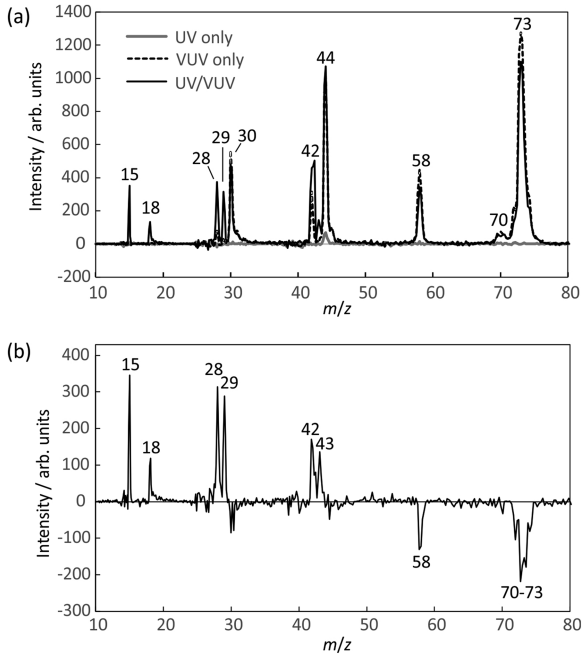

FIG. 3. (a) Time-of-flight mass spectra recorded with 118 nm pump only, 193 nm probe only, and with pump and probe lasers; (b) background subtracted time-of-flight spectrum showing the true two-colour pump-probe signal. See text for detailed discussion.

When the sample is illuminated by both the pump and probe lasers, new peaks appear at $m/z = 15$, 18, 28, and 29. In addition, the peaks assigned above to the probe-laser dissociative ionization are all attenuated, since neutral dissociation of *N*,*N*-DMF by the pump laser reduces the number of parent molecules available to undergo dissociative ionization. The true pump-probe signal, generated when neutral products of 193 nm laser photolysis are subsequently ionized by the 118 nm probe laser, is found by subtracting the "pump-only" and "probe-only" signals from the pump-probe signal and is shown in Fig. 3(b). The products of the parent molecule dissociative ionization appear as negative peaks, due to the previously noted attenuation of these signals when some of the parent molecules are dissociated by the 193 nm pump laser. The pump-probe signals of interest appear as positive peaks at $m/z = 15$, 18, 28, 29, 42, and 43. The corresponding velocity-map images, with pump-only and probe-only "background" signal already subtracted, are shown in Fig. 4, along with the speed distributions and velocity-dependent recoil anisotropy parameters, $\beta(v)$, extracted from the images. Values for β averaged over the velocity distribution for each fragment are shown in Table II.

As noted previously, following absorption of a 193 nm photon, *N*,*N*-dimethylformamide is expected to dissociate via cleavage of either the N—CO "peptide" bond, an N—CH_3 bond, or the aldehydic C—H bond. We consider each of these in turn in the light of the data presented in Figs. 3 and 4 and the potential energy curves presented in Sec. III A.

C. N—CO "peptide" bond cleavage

As summarised in Sec. I, previous experimental and theoretical studies of *N*,*N*-DMF photolysis[3–5] have proposed several pathways for cleavage of the N—CO "peptide" bond,

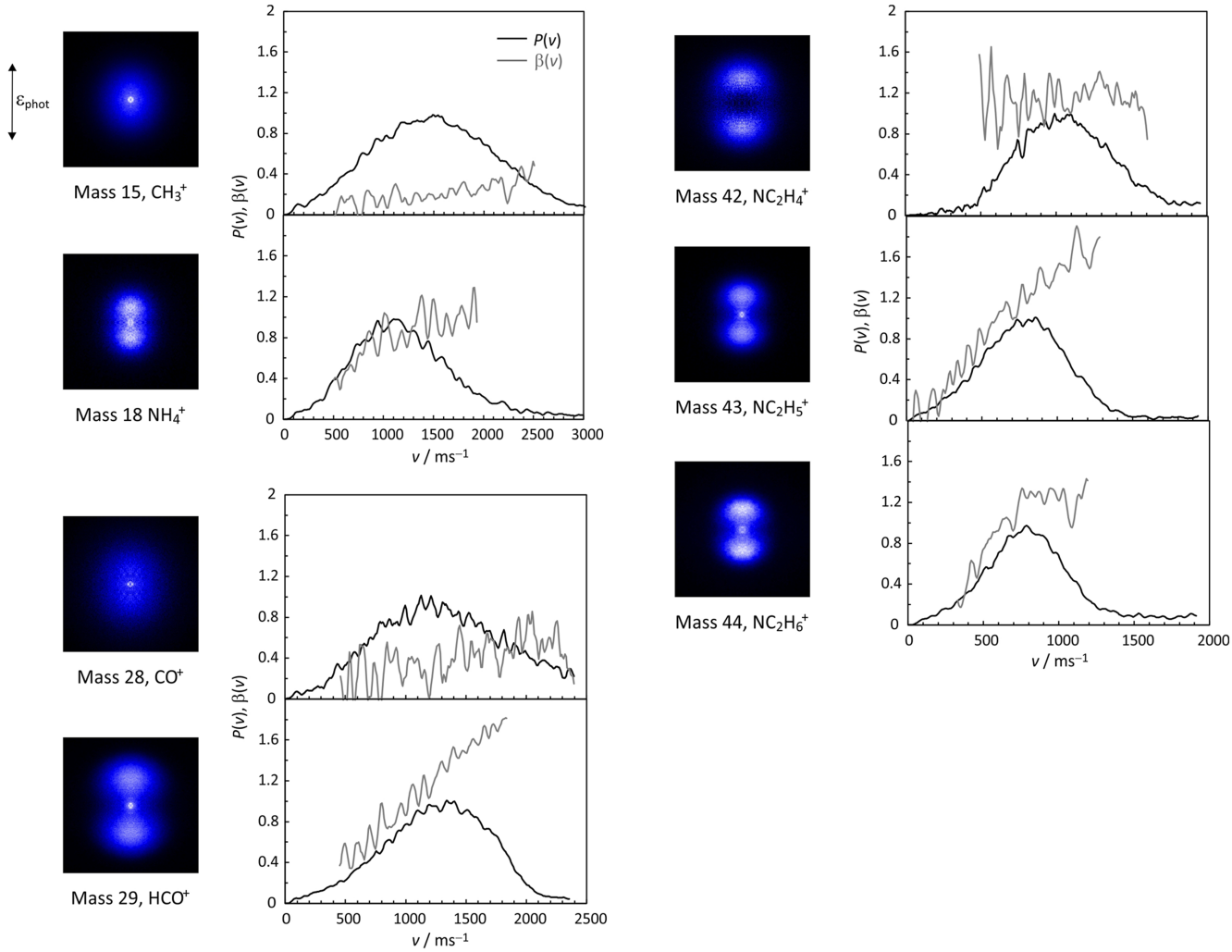

FIG. 4. Top: Background-subtracted velocity-map images for the fragments with $m/z = 15$, 18, 28, 29, 42, and 43, and one-laser velocity-map image for the $m/z = 44$ fragment, together with the corresponding speed distributions, $P(v)$, and velocity-dependent recoil anisotropy parameters, $\beta(v)$. Speed distributions have been normalised to a peak value of unity.

leading to the formation of HCO and $N(CH_3)_2$ products in various combinations of their ground and first-excited electronic states. Following cleavage of the N—CO bond, we therefore expect to observe signals in the time-of-flight mass spectrum corresponding to the HCO and $N(CH_3)_2$ products at $m/z = 29$ and 44, respectively. Unfortunately, the situation is a little more complicated than this due to neutral dissociation of a portion of the nascent HCO fragments and dissociative ionization of the $N(CH_3)_2$ fragments. However, we can still piece together the signals arising from this pathway. As noted previously, in the absence of the 118 nm laser, we observe a small signal at $m/z = 44$, attributed to the $N(CH_3)_2$ products of the N—CO bond cleavage that have been ionized by further photons from the 193 nm pump laser. The velocity-map image for these fragments is shown in Fig. 4 and exhibits a strong alignment of the product velocities parallel to the laser polarisation axis. The velocity-averaged recoil anisotropy parameter, β, is 0.92, but as can be seen in Fig. 4, and β increases steadily from small values at low velocities to almost its limiting value of +2 for the fastest fragments. A positive value of β is expected if the dissociation is rapid, given that the transition dipole moment for the (assumed) dominant $\pi^* \leftarrow \pi$ transition lies roughly parallel to the breaking N—CO bond (see Fig. 1). The increase in β with the photofragment velocity implies that while the axial recoil approximation holds for the fragments formed with the highest kinetic energy releases, it breaks down for slower fragments, reducing the value of β. This will be discussed in more detail later.

The $m/z = 44$ image discussed above was recorded with the 193 nm pump radiation alone. Upon introduction of

TABLE II. Beta parameters averaged over the product speed distribution. Estimated uncertainties in the last two digits based on one standard deviation of the difference between $\beta(v)$ (plotted in Fig. 4) and a polynomial fit through the data are given in parentheses.

Species	m/z	β
CH_3^+	15	0.19(07)
NH_4^+	18	0.76(15)
CO^+	28	0.34(16)
HCO^+	29	1.19(08)
$NC_2H_4^+$	42	1.05(16)
$NC_2H_5^+$	43	1.12(12)
$N(CH_3)_2^+$	44	0.92(09)

the 118 nm probe laser, the signal at $m/z = 44$ disappears, and instead, signals associated with the N—CO dissociation pathway can be identified at $m/z = 18$, 28, 29, 42, and 43. Based on the masses, ionization energies of the corresponding neutrals, and velocity-map images, the signals at $m/z = 18$, 42, and 43 can be assigned as $NC_2H_5^+$, $NC_2H_4^+$, and NH_4^+ products of dissociative ionization of the $N(CH_3)_2$ fragment, respectively, while the HCO^+ fragment appears at $m/z = 29$. The energetics preclude the observed CO^+ ions at $m/z = 28$ being dissociative ionization products of HCO, and as we will discuss below, we believe instead that a portion of the more internally excited neutral HCO fragments undergo neutral dissociation to H + CO, whereby a portion of CO is ionized by a combination of 193 nm and 118 nm photons.

We consider first the $N(CH_3)_2$ fragments and their dissociative ionization products. Previous studies[27] have shown a propensity for more highly internally excited $N(CH_3)_2^+$ ions to dissociate via H-atom loss to give $m/z = 43$ daughter ions, while $N(CH_3)_2^+$ ions with less internal energy lose H_2 to yield daughter ions with $m/z = 42$. The present study appears to corroborate this finding. The velocity-map image for the $NC_2H_5^+$ fragments ($m/z = 43$) is almost identical to that for the mass 44 fragments detected in the absence of the 118 nm light. In contrast, the velocity-map image for the $NC_2H_4^+$ fragments ($m/z = 42$) corresponds to fragments with significantly higher average velocities and therefore lower internal energies; in fact, the image has a clear "hole" in the center, indicating that it contains no contribution at all from the most highly internally excited products. The NH_4^+ ($m/z = 18$) fragments exhibit a similar angular distribution to that of the heavier fragments, indicating that the considerable rearrangement required for the formation of NH_4^+ results in little additional kinetic energy release on dissociation.

The signal arising from the HCO co-product appears at $m/z = 29$ (HCO^+) and 28 (CO^+). The 10.48 eV energy of a 118 nm photon exceeds the 8.83 eV ionization energy of HCO, but is well below the 13.79 eV ionization energy of CO. The observed CO^+ signal is thus unlikely to arise from the neutral CO[X] products of *N*,*N*-DMF photolysis. Instead, based on the relatively low kinetic energy release revealed by the velocity-map image of the m/z 28 ions relative to the HCO^+ ions, we conclude that the observed CO^+ signal arises from the predissociation of internally excited HCO products, followed by ionization of the resulting neutral CO fragments.

With a few assumptions, it is possible to reconstruct the momentum distributions of the nascent $N(CH_3)_2$ and HCO fragments from the velocity-map images of the various detected secondary fragment ions. Considering first the $N(CH_3)_2$ product, we assume that the loss of H or H_2 from $N(CH_3)_2$ during the dissociative ionization process and from HCO during predissociation does not greatly affect the velocity of the remaining fragment (since the very light H or H_2 carries away the bulk of the kinetic energy associated with the dissociation) and also that there is little further kinetic energy release when $N(CH_3)_2^+$ dissociates to form NH_4^+. The sum of the velocity-map images and momentum distributions for the mass 18, 42, and 43 fragments, weighted according to the relative intensities of their time-of-flight signals, should therefore recreate the momentum distribution of the nascent $N(CH_3)_2$ fragments.

Considering now the HCO products, the relative ionization efficiencies, and therefore detection efficiencies, of the nascent HCO and its predissociation product CO are unknown. However, a suitably weighted sum of the HCO and CO momentum distributions should reproduce the momentum distribution deduced for the $N(CH_3)_2$ fragments and their dissociative ionization products. Serendipitously, it appears that the CO and HCO ionization probabilities are similar under our experimental conditions and that the best momentum matching with the $N(CH_3)_3$ fragments is obtained by summing the momentum distributions for the $m/z = 29$ and 30 fragments, again weighted simply according to the intensities of their time-of-flight signals.

The summed velocity-map images and momentum distributions are shown in Fig. 5. Note that when calculating the relevant momenta, we have used the mass of the nascent HCO ($m/z = 29$) fragment to calculate the momenta associated with the $m/z = 28$ and 29 fragments and the mass of the nascent $N(CH_3)_2$ ($m/z = 44$) fragment to calculate the momenta associated with the $m/z = 18$, 42, and 43 fragments. There is almost perfect momentum matching between the reconstructed distributions for the HCO and $N(CH_3)_2$ fragments, as should be the case for the products of a two-body dissociation. The level of agreement between the two momentum distributions serves to confirm that we have correctly identified the various fragmentation processes giving rise to the observed signals.

We will now consider in more detail the product angular and kinetic energy distributions following the N—CO bond cleavage. The velocity-dependent β parameters extracted from all of the images (see Fig. 4) increase with fragment velocity,

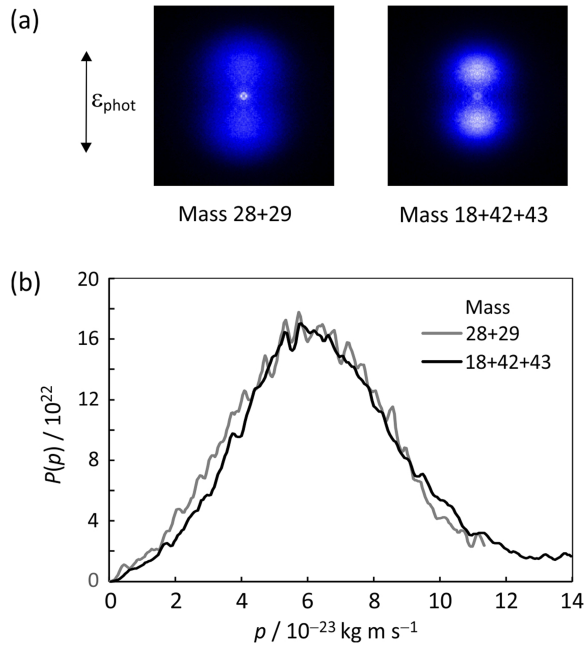

FIG. 5. (a) Summed velocity-map images and (b) summed momentum distributions, $P(p)$, for the fragments arising from the N—CO "peptide" bond fission, showing almost exact momentum matching. The momentum distributions have been normalised to the unit area under the curve.

approaching a limiting value of 2 for the fastest fragments detected at masses 29 and 43. The finding that β varies with the recoil velocity is reminiscent of previous observations for the $H + NH_2$ products arising in the near UV photolysis studies of NH_3,[28,29] and can be traced to the spread of out-of-plane motions in the dissociating molecules. The potential energy curves shown in Fig. 2(a) and the previous studies of Eckert-Maksić and Antol[5] highlight several regions where the topography of the potential energy surfaces will encourage the out-of-plane motion in concert with the N—CO bond extension. The initial excitation to any of the three accessible states, $1^1A''$, $2^1A'$, or $3^1A'$, each of which has non-planar minimum energy geometries, rapidly leads to population in the $1^1A''$ state via radiationless transfer first to the $2^1A'$ state and then at the $2^1A'/1^1A''$ conical intersection (TS1 in Ref. 5). Accessing these conical intersections requires an out-of-plane coupling mode, as does any subsequent transfer at the $1^1A''/1^1A'$ conical intersection (MXS1 in Ref. 5). Eckert-Maksić and Antol highlight the "significant reduction of pyramidalisation at the C and the N atoms of the peptide moiety at MXS1 and the shortening of the C=O bond as compared with TS1." Thus we can picture the *N*,*N*-DMF molecules approaching the final $1^1A''/1^1A'$ conical intersection with a range of out-of-plane momenta. Those molecules that happen to have near-planar geometries as they reach this region of the configuration space will follow the $1^1A''$ path through the conical intersection and dissociate to ground state products. Even in this limit, we can envisage a spectrum of outcomes. If the molecule is near planar and has little out-of-plane nuclear motion, then most of the available energy will be released in the form of product translation, and the recoil anisotropy will approach the limiting value given by the axial recoil approximation (in this case $\beta = +2$). Conversely, if the molecule just happens to be near-planar at the relevant point in configuration space but while executing a large amplitude out-of-plane (umbrella-like) vibration, the forces acting during dissociation will lead to rotational and vibrational internal excitations of the product, with a corresponding reduction in its kinetic energy, greater deviation from axial recoil, and a reduction in β. At the other extreme, *N*,*N*-DMF molecules that sample the conical intersection at very non-planar geometries will tend to follow the adiabatic path to the $N(CH_3)_2[\tilde{X}] + HCO[\tilde{A}]$ products; these products must recoil with much less kinetic energy along trajectories that are much farther from the axial recoil limit.

Considering now the photofragment kinetic energy distributions, Fig. 6(a) shows the total kinetic energy release (TKER) distribution determined from the momentum distributions in Fig. 5, together with the fitted TKER distributions for the "fast" and "slow" product channels obtained in the previous experimental study by Forde *et al.*[3] The distribution peaks at relatively low kinetic energy release, with a mean fraction of the available energy released into translation of $\langle f_T \rangle = 0.30$, but with a long tail that extends out to relatively high energies. This is consistent with the excitation of a variety of out-of-plane motions, as discussed above.

Maximum kinetic energy releases for the $HCO[\tilde{X}] + N(CH_3)_2[\tilde{X}]$, $HCO[\tilde{A}] + N(CH_3)_2[\tilde{X}]$, and $HCO[\tilde{X}] + N(CH_3)_2[\tilde{A}]$ channels are 2.53 eV, 1.38 eV, and 0.94 eV,

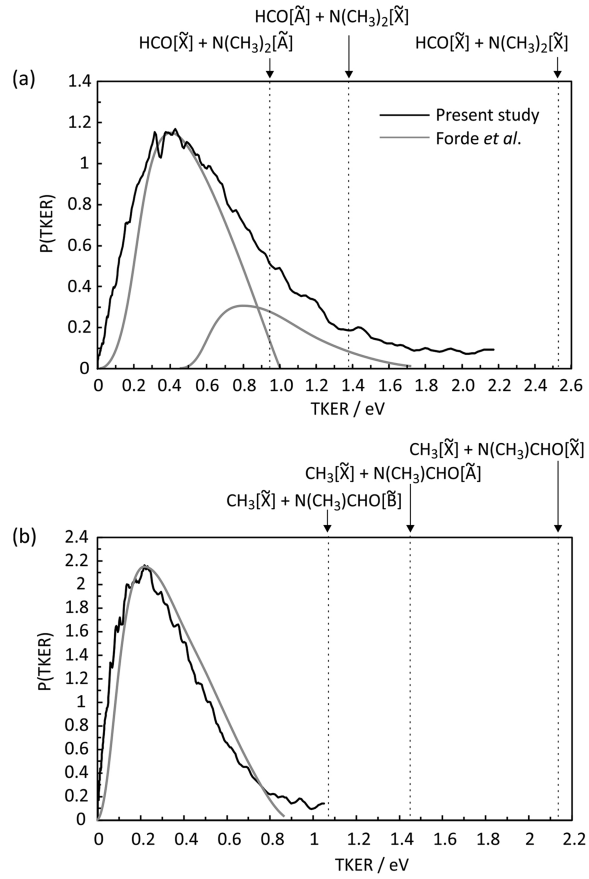

FIG. 6. Normalised total kinetic energy release distributions for (a) the N—CO "peptide" bond fragmentation channel and (b) the $N—CH_3$ bond fission channel following the 193 nm excitation of *N*,*N*-DMF. The fitted TKER distributions determined in a previous experimental study by Forde *et al.*[3] are superimposed on the data from the present study. Energetic limits for the formation of products in various electronic states are indicated.

respectively, and are shown as vertical dotted lines on the plot. These have been derived using the N—CO bond strength of 3.89 eV and provisional $N(CH_3)_2$ [Ã-X̃] splitting of 1.59 eV reported by Forde *et al.*[3] and the well-established energy[26] of the HCO[Ã] state of 1.15 eV.

The TKER distribution obtained from our data is in almost quantitative agreement with the fitted distributions determined by Forde *et al.*,[3] but provides no real further insights into the validity or otherwise of the previously proposed decomposition into "fast" and "slow" TKER components associated with the formation of X̃ and Ã state $N(CH_3)_2$ fragments. The present data show no obvious discontinuity in either the product yield or the recoil anisotropy (β) parameter in the vicinity of the predicted threshold energies for forming electronically excited products. In our earlier discussion of the observed β parameters in the light of the potential energy curves shown in Fig. 2(a), we identified motions orthogonal to the N—CO bond extension as likely sources of product internal excitation, and noted opportunities for branching between diabatic potential energy surfaces (and thus for forming different asymptotic products) at both the $2^1A'/1^1A''$ and $1^1A''/1^1A'$ conical intersections. We suggest that the electronic branching in these products remains a somewhat open question, which might be addressable through experiments at

other excitation wavelengths (such experiments are currently underway in our laboratory) or by the state-of-the-art quantum dynamics simulations.

D. N—CH_3 bond cleavage

Of the two products arising from the N—CH_3 bond cleavage, CH_3 can be ionized at 118 nm, while $HCONCH_3$ cannot. A relatively intense peak corresponding to the CH_3^+ ion is present at $m/z = 15$ in the time-of-flight spectrum [see Fig. 3(b)], indicating that the N—CH_3 bond cleavage channel is active. As expected, no signal is observed at $m/z = 58$ for the $HCONCH_3$ cofragment.

The velocity-map image for the CH_3 fragment shows a relatively isotropic angular distribution ($\beta = 0.19$). Small values of β can often be explained in terms of a slow or delayed dissociation process. This is unlikely in the present case given both the topology of the calculated potential energy curves and the fact that the N—CH_3 bond cleavage must be kinetically competitive with the N—CO bond cleavage. Instead, our favored explanation is that the near-zero value of β arises simply from the molecular geometry. The molecular geometry implies that the N—CH_3 bond cleavage will lead to the release of a CH_3 fragment at an angle of approximately 60° to the N—CO bond axis. The transition dipole for the dominant $\pi^* \leftarrow \pi$ transition to the $3^1A'$ state lies almost parallel to the N—CO bond axis. In molecules that absorb a photon and dissociate, there will therefore be an approximately $\cos^2$ distribution of the N—CO axis relative to the photolysis laser polarisation vector. A simple model combining this $\cos^2$ distribution of the N—CO bond axis with the (near magic-angle) ejection directions of the CH_3 fragments predicts an almost isotropic distribution of CH_3 photofragments about the laser polarisation axis, as observed.

Figure 6(b) compares the total kinetic energy release distribution determined from the CH_3 velocity-map image with the fitted TKER distribution obtained in the earlier experiments by Forde *et al.*[3] As for the N—CO channel, the two sets of data, recorded using different experimental techniques, are in remarkably good agreement. Forde *et al.*[3] assigned at least some of their CH_3 signals to cracking products of larger photofragments, particularly $N(CH_3)_2$, resulting from the 200 eV electron ionization within their detector. However, we do not believe this to be the case in our experiments, which employs "soft" 118 nm photoionization. The excess energy of 0.59 eV following the 118 nm photoionization of $N(CH_3)_2$ is considerably less than ~3.9 eV[26] required for fragmentation into $NCH_3 + CH_3^+$ products.

The dotted vertical lines in Fig. 6(b) indicate the maximum kinetic energy releases associated with CH_3 partnered by $HCONCH_3$ in its $\tilde{X}$, $\tilde{A}$, and $\tilde{B}$ states, the three channels predicted by the CASPT2 calculations to be energetically accessible at 193 nm. The measured kinetic energy release distribution does not extend beyond the energetic threshold for the formation of $CH_3[\tilde{X}]$ + $HCONCH_3[\tilde{B}]$ products. With reference to the potential energy curves shown in Fig. 2(b), it is therefore tempting to suggest that most *N*,*N*-DMF ($2^1A'$) molecules that dissociate by the N—CH_3 bond fission avoid the $2^1A'/1^1A''$ conical intersection at small bond extensions and follow the adiabatic path to electronically excited ($\tilde{B}$ state) $HCONCH_3$ radical products. However, we also recognise that arguments based solely on an observed cutoff in a kinetic energy release spectrum fail if much of the available energy is partitioned into internal excitation of the products. The present data therefore does not exclude the formation of internally excited $\tilde{X}$ or $\tilde{A}$ state $HCONCH_3$ products. Liu *et al.*[4] invoked intersystem crossing to the lowest triplet potential energy surface to explain the formation of CH_3 radical products. However, neither the observed total kinetic energy release data nor the competitiveness of the N—CH_3 bond fission process with fast N—CO bond fission would appear to sit comfortably with such a mechanism.

E. C—H bond cleavage

A photon of wavelength 118 nm provides insufficient energy to ionize atomic hydrogen, but according to the calculated ionization energies reported in Table I, should suffice to ionize and detect the $CON(CH_3)_2$ cofragment. However, we see no evidence in the time-of-flight spectrum for the formation of this product. While secondary dissociation of the $CON(CH_3)_2$ products to $CO + N(CH_3)_2$ is energetically possible at 193 nm, we also see no evidence for the $H + CON(CH_3)_2$ pathway in the H-atom Rydberg tagging photofragment translational spectroscopy experiments. Dissociative ionization of $CON(CH_3)_2$ at 118 nm to form $CO^+ + N(CH_3)_2$ or $CO + N(CH_3)_2^+$ is not energetically possible, so we do not expect to see products from this channel at other masses. We therefore conclude that the C—H bond cleavage is too slow to compete with rival photofragmentation pathways following photoexcitation of *N*,*N*-DMF at 193 nm. From the potential energy curves shown in Fig. 2(c), we see that the aldehydic C—H bond fission requires radiationless transfer to the triplet continuum, so the non-observation of these pathways lends further support to the view that intersystem crossing is unlikely to be competitive with the fast rates of N—CO and N—CH_3 bond fission on the singlet potential energy surfaces.

Though we have ruled out the H + $CON(CH_3)_2$ fragmentation pathway, we do detect atomic hydrogen fragments in the H-atom Rydberg tagging photofragment translational spectroscopy measurements described in Sec. II A. The measured H atom flight times t can be converted to a total kinetic energy release distribution using the expression

$$\mathrm{TKER} = \frac{1}{2} m_H \left(1 + \frac{m_H}{m_R}\right) \left(\frac{d}{t}\right)^2, \quad (1)$$

where m_H and m_R are the masses of the H atom and radical cofragment, respectively, and d is the distance between the interaction region and the detector (36.9 cm in the present experiments). We have used $m_R = 72.09$ u, the value appropriate for the radical product formed upon the C—H bond fission in *N*,*N*-DMF. However, the H atom is much lighter than any of the possible cofragments that the factor $(1 + m_H/m_R)$ is always close to unity, and the choice of the cofragment therefore has little effect on the time-of-flight to TKER conversion.

The TKER distribution for H atoms detected following the photolysis of *N*,*N*-DMF at 193 nm is shown in Fig. 7.

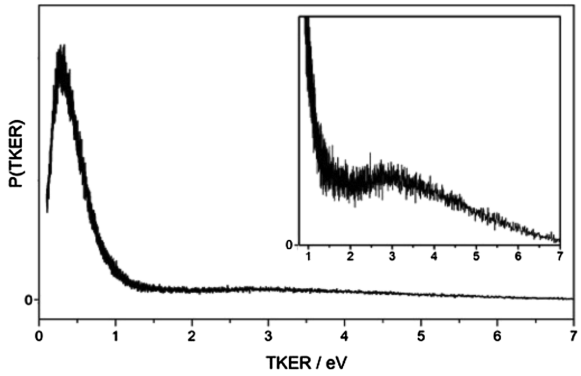

FIG. 7. Total kinetic energy release (TKER) distributions derived from measured times-of-flight of H atoms formed in the 193 nm photolysis of *N*,*N*-DMF. The inset shows the high-TKER data plotted on an eight-times expanded vertical scale.

The distribution comprises a relatively narrow peak centered at ~0.5 eV and extending beyond 1.5 eV, atop a much broader peak that extends out to beyond 6.0 eV. The low-TKER peak varies little with changes in laser polarisation or wavelength over the range from 193.3 nm to 243.1 nm. This suggests that these H atoms arise either from the unimolecular decay of highly internally excited ground-state *N*,*N*-DMF formed following internal conversion from the initially excited electronic states or from the unimolecular decay of highly internally excited molecular fragments formed in the primary dissociation process (e.g., the HCO fragments arising from the $N(CH_3)_2$ + HCO channel). The fast component of the distribution extends to kinetic energies far greater than could result from the C—H bond fission within either the CHO or CH_3 groups of *N*,*N*-DMF, but would be consistent with the secondary photolysis of HCO radicals formed in the primary N—CO bond fission process. HCO is known[30] to absorb via the $\tilde{B} \leftarrow \tilde{X}$ transition at 193 nm. The H—CO bond dissociation energy[31] of 0.66 ± 0.04 eV, coupled with the 6.42 eV photon energy, implies an upper limit for the TKER of around 5.76 eV, or higher if the HCO fragments are formed with internal excitation. This value matches well with the observed onset of the broad peak in the TKER distribution derived from the H atom time-of-flight data. The fact that the derived TKER distribution can be rationalised simply in terms of dissociation of internally "hot" *N*,*N*-DMF parent molecules and/or primary molecular fragments, together with the secondary photolysis of primary HCO products, reinforces the conclusion from the velocity-map imaging study that the C—H bond cleavage is not an important primary process in the 193 nm photolysis of *N*,*N*-DMF.

IV. CONCLUSIONS

We have presented data from a comprehensive experimental and theoretical study into the photofragmentation dynamics of *N*,*N*-dimethylformamide at 193 nm. In our velocity-map imaging experiments we observe two main fragmentation channels: cleavage of the N—CO "peptide" bond to form HCO and $N(CH_3)_2$ products and CH_3 loss. We also see some evidence for H atom formation, with both "slow" and "fast" contributions to the H atom system. We tentatively ascribe the slow H atoms as resulting from unimolecular decay of highly vibrationally excited parent *N*,*N*-DMF molecules formed by internal conversion from the photoexcited state(s) and/or from predissociation of nascent internally excited HCO. Fast H atoms are thought to result from the secondary photolysis of the primary HCO photoproducts. In the case of "peptide" bond fission, our data are consistent with initial population primarily of the $3^1A'$ state of the parent, followed by sequential internal conversion to the $2^1A'$ and $1^1A''$ states, the latter of which correlates with the ground state HCO and $N(CH_3)_2$ products. This has been identified as the dominant fragmentation pathway in two previous theoretical studies.[4,5] Both studies also identified minor pathways leading to formation of either $N(CH_3)_2$ or HCO in their first electronically excited states. While our measured product total kinetic energy release distributions would certainly be consistent with small contributions from these pathways, we see no clear evidence for them in our data. Our experimental data are in very good agreement with data recorded by Forde *et al.*[3] in their earlier experimental study on *N*,*N*-DMF photofragmentation. However, in contrast to the conclusions drawn in earlier study, we see no need to invoke two different fragmentation pathways in order to explain our observed total kinetic energy release distributions. The products of the N—CO bond fission pathway appear to be formed with significant internal excitation, consistent with rapid impulsive breaking of the bond.

The CH_3 loss channel is also thought to involve a sequence of radiationless transitions following initial population of the $3^1A'$ state, with initial transfer to the $2^1A'$ state followed either by dissociation on this potential energy surface or radiationless transfer to the $1^1A''$ state. The adiabatic potentials for these two states (see Fig. 2) correlate to the ground-state CH_3 partnered by $HCONCH_3$ in its second excited [$\tilde{B}$] or ground [$\tilde{X}$] electronic state, respectively. The TKER distribution for this channel does not extend beyond the energetic limit for formation of the $CH_3[\tilde{X}] + HCONCH_3[\tilde{B}]$ products, so it would certainly be consistent with dissociation on the $2^1A'$ surface. Dissociation to form ground-state products is also consistent with the data, in which case the measured TKER distribution implies a high degree of product vibrational or rotational excitation.

We see no evidence for direct H atom loss channels from the excited-state *N*,*N*-DMF in either our velocity-map imaging data or in data from separate H-atom Rydberg tagging photofragment translational spectroscopy measurements. However, as noted above, we do see some evidence for H loss following internal conversion of electronically excited parent or fragment molecules to highly vibrationally excited levels of the respective ground states, as well as observing H atoms from the secondary photolysis of HCO fragments formed through the N—CO bond fission.

In the future, we plan to study *N*,*N*-DMF photolysis at additional wavelengths within the ultraviolet, as well as investigating a series of related molecules in order to determine whether the fragmentation pathways observed in the present study are common to other small peptide-bond-containing species.

ACKNOWLEDGMENTS

We gratefully acknowledge funding via the ERC grant ImageMS and the EPSRC, Grant Nos. EP/G00224X/1 and EP/L005913/1.

[1] J. S. Brodbelt, J. Am. Soc. Mass Spectrom. **22**, 197 (2011).
[2] N. R. Forde, T. L. Myers, and L. J. Butler, Faraday Discuss. **108**, 221 (1997).
[3] N. R. Forde, L. J. Butler, and S. A. Abrash, J. Chem. Phys. **110**, 8954 (1999).
[4] D. Liu, W. Fang, Z. Lin, and X. Fu, J. Chem. Phys. **117**, 9241 (2002).
[5] M. Eckert-Maksić and I. Antol, J. Phys. Chem. A **113**, 12582 (2009).
[6] H. D. Hunt and W. T. Simpson, J. Am. Chem. Soc. **75**, 4540 (1953).
[7] K. Kaya and S. Nagakura, Theor. Chim. Acta **7**, 117 (1967).
[8] L. Serrano-Andrés and M. P. Fülscher, J. Am. Chem. Soc. **118**, 12190 (1996).
[9] R. Liu and P. Pulay, J. Comput. Chem. **13**, 183 (1992).
[10] X. Qiu, Z. Ding, Y. Xu, Y. Wang, and B. Zhang, Phys. Rev. A **89**, 033405 (2014).
[11] W. S. Hopkins, M. L. Lipciuc, S. H. Gardiner, and C. Vallance, J. Chem. Phys. **135**, 034308 (2011).
[12] S. H. Gardiner, T. N. V. Karsili, M. L. Lipciuc, E. Wilman, M. N. R. Ashfold, and C. Vallance, Phys. Chem. Chem. Phys. **16**, 2167 (2014).
[13] A. H. Kung, J. F. Young, and S. E. Harris, Appl. Phys. Lett. **22**, 301 (1973).
[14] A. H. Kung, J. F. Young, and S. E. Harris, Appl. Phys. Lett. **28**, 294 (1976).
[15] N. P. Lockyer and J. C. Vickerman, Laser Chem. **17**, 139 (1997).
[16] V. Dribinski, A. Ossadtchi, V. A. Mandelshtam, and H. Reisler, Rev. Sci. Instrum. **73**, 2634 (2002).
[17] A. J. T. B. Eppink and D. H. Parker, Rev. Sci. Instrum. **68**, 3477 (1997).
[18] B. Cronin, M. Nix, R. Qadiri, and M. N. R. Ashfold, Phys. Chem. Chem. Phys. **6**, 5031 (2004).
[19] M. J. Frisch, G. W. Trucks, H. B. Schlegel, G. E. Scuseria, M. A. Robb, J. R. Cheeseman, G. Scalmani, V. Barone, G. A. Petersson, H. Nakatsuji, X. Li, M. Caricato, A. Marenich, J. Bloino, B. G. Janesko, R. Gomperts, B. Mennucci, H. P. Hratchian, J. V. Ortiz, A. F. Izmaylov, J. L. Sonnenberg, D. Williams-Young, F. Ding, F. Lipparini, F. Egidi, J. Goings, B. Peng, A. Petrone, T. Henderson, D. Ranasinghe, V. G. Zakrzewski, J. Gao, N. Rega, G. Zheng, W. Liang, M. Hada, M. Ehara, K. Toyota, R. Fukuda, J. Hasegawa, M. Ishida, T. Nakajima, Y. Honda, O. Kitao, H. Nakai, T. Vreven, K. Throssell, J. A. Montgomery, Jr., J. E. Peralta, F. Ogliaro, M. Bearpark, J. J. Heyd, E. Brothers, K. N. Kudin, V. N. Staroverov, T. Keith, R. Kobayashi, J. Normand, K. Raghavachari, A. Rendell, J. C. Burant, S. S. Iyengar, J. Tomasi, M. Cossi, J. M. Millam, M. Klene, C. Adamo, R. Cammi, J. W. Ochterski, R. L. Martin, K. Morokuma, O. Farkas, J. B. Foresman, and D. J. Fox, GAUSSIAN 09, Revision A.02, Gaussian, Inc., Wallingford, CT, 2016.
[20] H. J. Werner, P. J. Knowles, G. Knizia, F. R. Manby, M. Schütz, P. Celani, T. Korona, R. Lindh, A. Mitrushenkov, G. Rauhut, K. R. Shamasundar, T. B. Adler, R. D. Amos, A. Bernhardsson, A. Berning, D. L. Cooper, M. J. O. Deegan, A. J. Dobbyn, F. Eckert, E. Goll, C. Hampel, A. Hesselmann, G. Hetzer, T. Hrenar, G. Jansen, C. Köppl, Y. Liu, A. W. Lloyd, R. A. Mata, A. J. May, S. J. McNicholas, W. Meyer, M. E. Mura, A. Nicklass, D. P. O'Neill, P. Palmieri, K. Pflüger, R. Pitzer, M. Reiher, T. Shiozaki, H. Stoll, A. J. Stone, R. Tarroni, T. Thorsteinsson, M. Wang, and A. Wolf, MOLPRO, version 2010.1, a package of *ab initio* programs, 2010.
[21] M. N. R. Ashfold, G. A. King, D. Murdock, M. G. D. Nix, T. A. A. Oliver, and A. G. Sage, Phys. Chem. Chem. Phys. **12**, 1218 (2010), and references therein.
[22] N. Hobday, M. S. Quinn, K. Nauta, D. U. Andrews, M. J. T. Jordan, and S. H. Kable, J. Phys. Chem. A **46**, 12091 (2013).
[23] C. L. Reed, M. Kono, S. R. Langford, T. W. R. Hancock, R. N. Dixon, and M. N. R. Ashfold, J. Chem. Phys. **106**, 6198 (1997).
[24] C. L. Reed, M. Kono, S. R. Langford, R. N. Dixon, and M. N. R. Ashfold, J. Chem. Soc., Faraday Trans. **93**, 2721 (1997).
[25] R. N. Dixon and T. W. R. Hancock, J. Phys. Chem. **101**, 7567 (1997).
[26] See http:webbook.nist.gov for Data from the NIST Chemistry Webbook.
[27] N. R. Forde, L. J. Butler, B. Ruscic, O. Sorkhabi, F. Qi, and A. G. Suits, J. Chem. Phys. **113**, 3088 (2000).
[28] D. H. Mordaunt, M. N. R. Ashfold, and R. N. Dixon, J. Chem. Phys. **104**, 6460 (1996).
[29] R. N. Dixon, Mol. Phys. **88**, 949 (1996).
[30] D. E. Milligan and M. E. Jacox, J. Chem. Phys. **51**, 277 (1969).
[31] J. Riedel, S. Dziarzhytski, A. Kuczmann, F. Renth, and F. Temps, Chem. Phys. Lett. **414**, 473 (2005).